

HIGH RESOLUTION HST-COS Ly α PROFILE

C. SCARLATA, M. HAYES, N. PANAGIA, L. COWIE AND ET AL.

Draft version May 11, 2016

ABSTRACT

Subject headings: galaxies: ISM — ISM: structure

1. INTRODUCTION

Ly α -based samples additionally carry the potential to constrain the epoch of cosmic reionization via an expected sharp drop in their number density as the ionization state of the intergalactic medium (IGM) changes (Miralda-Escudé & Rees 1998, Malhotra & Rhoads 2006). However, this interpretation hinges on a complete understanding of the Ly α escape physics, and on the evolution of the intrinsic properties of the Ly α emitter population as a function of redshift.

An ultraviolet resonant line such as Ly α is highly sensitive to the relative geometry and kinematics of the gas and dust, which is bound to change when subject to the dynamical effects of the increased merger rate with increasing redshift, as well as the varying and observationally undetermined H I content of galaxies. Most of our knowledge comes from small, non-representative samples of Ly α emitters at $z = 0$, and from cosmological populations of Ly α emitters ($z > 2$, for which the supplementary observations required to characterize galaxy physical properties, such as optical emission lines, are redshifted to expensive and/or inaccessible wavelengths). Therefore, a comprehensive study of the astrophysics behind the Ly α production, transport, and escape has not so far been made. This presents a fundamental limitation to our ability to use the Ly α emission as a cosmological tool.

We use a standard $H_0 = 70 \text{ km s}^{-1} \text{ Mpc}^{-1}$, $\Omega_M = 0.3$, and $\Omega_\Lambda = 0.7$ cosmology.

2. THE SAMPLE

The targets for the HST COS spectroscopic followup are taken from the sample of Ly α emitters identified by Deharveng et al. (2008) and Cowie et al. (2010) in deep GALEX grism spectroscopy. The GALEX sample includes 119 Ly α emitters, 49 of which have rest-frame Ly α emission line EW $> 20 \text{ \AA}$. From the parent sample of GALEX Ly α emitters, we originally selected 25 galaxies that satisfied the following criteria: 1) are classified as star-forming based on optical emission line ratios (e.g., Cowie et al. 2010), 2) have Ly α emission line rest-frame EW $> 20 \text{ \AA}$ in the low resolution GALEX spectra, and 3) have redshift confirmed using optical spectroscopy. As we show in Scarlata et al. (2009), Atek et al. (2009), Finkelstein et al. (2009), and Cowie et al. (2010), the requirement of having the optical confirmation does not change the target selection function of the sample, since 100% of the sources we followed up were, in fact, confirmed. High redshift Ly α emitters are usually selected with Hu et al.’s (1998) definition that they have a rest frame EW greater than 20 \AA (see also Kornei et al. 2010). Thus, the EW cut ensures that we are able to make a valid comparison with the samples of Ly α emitters selected at $z > 2$.

3. OBSERVATIONS AND DATA ANALYSIS

The galaxies were observed with the Cosmic Origins Spectrograph (COS) on the *Hubble Space Telescope* (HST). Imaging target acquisition for COS observations requires a S/N of forty over a small aperture – implying substantial overheads on the spectroscopic observations, particularly for NUV faint and/or diffuse targets. In order to avoid continuum biases and limit the total observing time, we chose to acquire on nearby bright stars for 22 out of the 25 target galaxies. We used the Primary Science Aperture (PSA) and Mirror A or B (depending on the star brightness). To limit positioning errors due to large telescope slews, we observed only galaxies for which the acquisition target was at a distance $\leq 2'$. The offsets between the acquisition star and the main target were computed from ground based imaging in most cases, while ACS HST imaging was used for three objects in the COSMOS field (see Table ??). In order to check the acquisition procedure, we obtained a direct NUV image of the aperture after the telescope was shifted to the target position. The exposure times of the images vary between 80 and 200 seconds, depending on the GALEX NUV magnitude of the target.

The target acquisition images are shown in Figure 1. Each stamp is oriented so that the dispersion direction is aligned with the horizontal axis. The large thick circle shows the full 1.²⁵-radius COS aperture, while the smaller one shows the unvignetted aperture (radius = 0.⁷) where the throughput is larger than 80% (?). For four galaxies (see Table ??) the star used for the acquisition was too bright to be observed with MIRRORA. In these cases we performed the acquisition using MIRRORB and changed to MIRRORA for the science exposures. Although the change from MIRRORB to MIRRORA does not affect a target’s relative location in the

² Space Telescope Science Institute, 3700 San Martin Drive, Baltimore, MD 21218, USA

³ Observatoire de Genève, 51, Ch. des Maillettes, CH-1290, Sauverny, Switzerland

⁴ California Institute of Technology, MS 105-24, Pasadena, CA91125

⁵ Max-Planck-Institut für extraterrestrische Physik, Giessenbachstrasse 1, 85748 Garching, Germany

⁶ Research School of Astronomy and Astrophysics, the Australian National University, Canberra 0200, Australia

⁷ INAF/Osservatorio Astrofisico di Catania, Via S.Sofia 78, I-95123 Catania, Italy

⁸ Department of Astronomy, University of Padova, Vicolo dell’Osservatorio 3, I-35122, Padova, Italy

⁹ Supernova Ltd., Olde Yard Village 131, Northsound Road, Virgin Gorda, British Virgin Islands

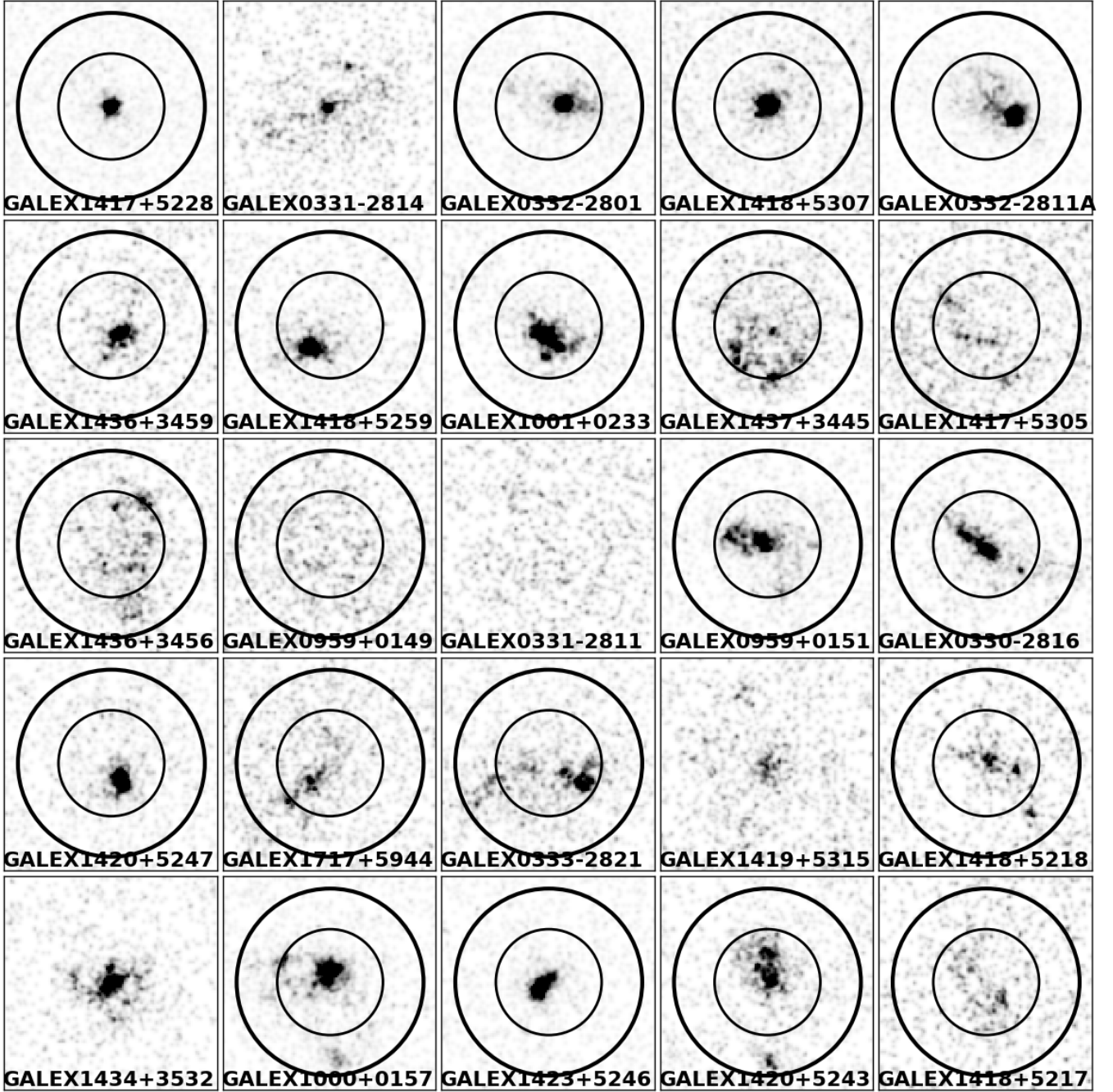


FIG. 1.— HST NUV images of the 25 sample galaxies observed with COS. The circle shows the position of the COS 2.5'' aperture on the object. For four galaxies the position could not be determined (see text for detail).

aperture, it does move the location of the aperture on the detector, making it impossible to measure the precise target's location in the aperture. For these objects we do not show the COS aperture, and center the stamp on the galaxy centroid measured directly on the NUV images. Figure 1 shows that the galaxy acquisition worked very well, with all galaxies falling in the unvignetted region defined above.

For each target, we obtained FUV medium resolution spectroscopy using the G160M grism in TIME-TAG mode, with typical exposure times of 2300s. We chose the grating central wavelength to ensure that the Ly α

would not fall in the wavelength gaps due to the physical layout of the detectors and the optics. In order to reduce the impact of microchannel plate detector fixed pattern noise, we took two exposures for each target, with FP-POS= 3 and FP-POS= 4, respectively. The wavelength range covered by the COS spectra is approximately 1405 – 1775Å, with a nominal dispersion of 12.23 mÅ px⁻¹. The effective spectral resolution, however, depends on the size of the object in the dispersion direction and vary from $\sim 0.035\text{Å}$ for a compact, point-like, source (e.g., GALEX1417+5228), to $\sim 0.7\text{Å}$

for a source filling the full unvignetted aperture (e.g., GALEX1436+3456).

We calibrated and extracted the COS spectra using `calcos` v2.15.4 task in `pyraf`. Due to the target acquisition strategy, the most galaxies were not perfectly centered in the COS aperture. This spatial offsets introduces a wavelength calibration shift that needs to be corrected in the calibration steps. We used the direct NUV images to measure the shifts in the dispersion direction between the position of the center of each galaxy and the expected position of the COS aperture center. The shifts ranged between -18 and 10 NUV pixels, with a standard deviation of 8 pixels (corresponding to 0.1\AA or $\approx 20 \text{ km s}^{-1}$ at the observed wavelength of Ly α). The correction to the wavelength zero point was applied to the wavelength column in the `corrtag` files, and `calcos` was run again with the edited files as input. This correction does not only take care of the wavelength zero point, but also allows us to apply the proper sensitivity at each wavelength. No correction could be applied to the four galaxies for which the acquisition was performed with MIRRORB. In these cases we added a systematic error component to the wavelength calibration, equal to the standard deviation of the galaxies' centers in the dispersion direction.

The PSA aperture throughput decreases toward the edges of the field of view, due to the increasing vignetting of the flux. This change in throughput is not accounted for in the `calcos` pipeline, which is optimized for point sources, and results in an underestimate of the extracted flux for extended sources. We scaled the extracted spectra by a correction factor computed using the direct imaging, and assuming that the aperture throughput is symmetric with respect to the aperture center. The scaling factors vary between 1.1 and 1.3 .

Because of the acquisition strategy, the vignetting correction may be significant even for compact sources, if the object was not perfectly centered within the aperture. Figure 2 (left panel) shows the comparison between the total aperture-corrected NUV flux measured in the $2''.5$ COS aperture and the GALEX NUV total flux. For each galaxy, we show the COS measurements before and after vignetting correction, and the size of the points is proportional to the measurement of the half-light-radius (see below). The solid line indicates the $1:1$ relation. Corrected fluxes in the small COS apertures show a broad agreement with the GALEX measurements, indicating that the objects do not have substantial amount of light falling outside the COS aperture. We do not see a systematic trend with galaxy size. We checked that for the typical NUV-I colors of our sources, the color term between the GALEX and COS magnitudes is negligible.

In Appendix ?? we show the full COS FUV segment (either A or B) covering the Ly α profiles. The spectra have been binned in order to increase their signal-to-noise ratio. We chose a bin-size of $10(20)$ pixels in the dispersion direction, corresponding to $XXX\text{\AA}(XXX\text{\AA})$. This bin size does not substantially decrease the effective spectral resolution of the data, which depends on the object size (in COS native pixels) in the dispersion direction. We computed the errors associated with the binned profiles following the procedure described in ?. Briefly, we used Poissonian statistic to compute the noise on the

observed total counts in each bin (from the GCOUNTS), following ?. We then computed the errors on the flux by dividing for the exposure time and the sensitivity curve.

3.1. Measurement of line flux and wavelength of line peak

Figure 5 shows the spectra of the GALEX sources centered around the position of the Ly α emission line. The line profiles are presented in velocity space, shifted into the rest-frame using the systemic velocity calculated from the H α emission line (see Table ??, for the source of the optical redshift). The profiles are characterized by complex structures and asymmetric shapes, often with multiple peaks. We compute the total Ly α flux within the aperture, by integrating the continuum-subtracted line profile between $\pm 2.5\text{\AA}$ from the expected line center. We estimated the continuum by computing the median flux density within 2\AA on both sides of the line center. The line-flux error was computed from the error spectrum derived during the spectral extraction process.

Low spectral resolution Ly α emission line profiles of high redshift galaxies, as well as of the majority of local massive galaxies show that the emission line is typically characterized by a single, broad, asymmetric peak typically redshifted with respect to the galaxy systemic velocity (??). Recent results from COS spectroscopy, however, showed that lower-mass, extreme emission line, compact galaxies have Ly α profiles characterized by both a prominent peak (redshifted w.r.t. the galaxy systemic velocity) but also a secondary emission peak, blueshifted w.r.t. the systemic velocity (??).

For each galaxy, we provide a measurement of the peak velocities in Table ???. Hereafter we follow the convention that blue(red) peak identify the peak on the blue(red) side of the Ly α wavelength expected from the H α redshift. We, when two peaks are present in the profile, λ_R refers to the wavelength of The peak wavelengths were derived by fitting a Gaussian function to a small wavelength range ($\pm 0.6\text{\AA}$) centered around the visually identified position of the peaks. For the four objects for which MIRROR-B was used in the acquisition process, errors in the peak wavelength include the 0.1\AA centering uncertainty. In order to compare with lower-resolution measurements we also compute the centroid wavelength of the line as:

$$\lambda_C = \frac{\sum f_\lambda v}{\sum f_\lambda}, \quad (1)$$

3.2. Size measurement and concentration

We use the COS images to measure galaxies' sizes in the NUV. Because of the complicated morphology of the star-forming regions in many of the galaxies, we cannot fit a smooth profile to the UV light distribution (e.g., GALEX1436–3456). We have therefore computed the radius of the circular aperture containing half of the total NUV flux, using a curve of growth analysis. The centers used for the circular apertures are indicated with a cross in Figure 1. Because of the small aperture of the COS instrument, we use the GALEX NUV luminosity as an estimate of the total light of the galaxy. Before computing the aperture flux, we multiplied each NUV image by the COS aperture response map to account for

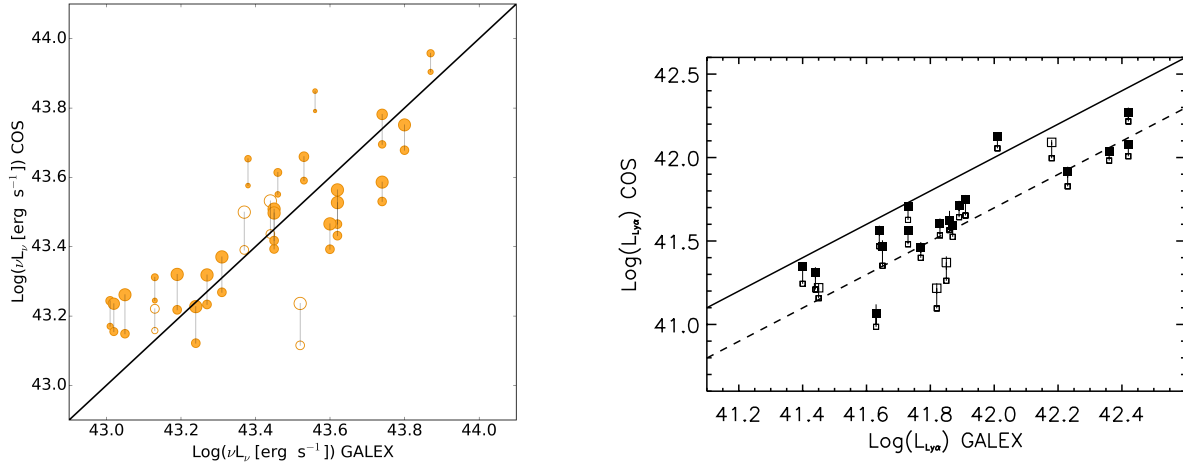


FIG. 2.— Comparison between the total luminosities as measured by GALEX and COS. The *Left* panel shows the continuum fluxes in monochromatic units, while the *Right* panel shows Ly α . Large points have been corrected using the aperture correction estimated from the UV continuum. Open large squares indicate galaxies observed with MIRROR-B. After the aperture correction, approximately 30% of the Ly α flux is missed by the 2''5 COS aperture, indicating that the Ly α emission is more extended than the continuum.

the decreasing throughput as function of the spatial offset from the aperture center (?). The half-light–radii are reported in Table ??.

4. RESULTS

4.1. UV-morphology

Being sensitive to light between 1600 and 3100Å, the COS NUV channel probes the continuum coming from hot young stars. Ly α is inside the NUV bandpass for only three of our galaxies, (those at $z > 0.31$), where the EW is anyway insufficient to dominate the global light, but could in principle extend the morphologies somewhat. Figure 1 we show the NUV COS images of the 25 galaxies, together with the position of the circular COS aperture (when it could be determined, see section 3). The galaxies show a variety of morphology in the NUV: in some objects (e.g., GALEX1417+5305) the UV light is distributed smoothly over a large part of the COS aperture (i.e., diffuse objects), in others (e.g., GALEX1417+5228) the light is concentrated in a single compact star cluster (i.e., compact objects), while in others (e.g., GALEX1000+0157) the light is distributed in multiple clumps. The morphological classification is reported in Table 2.

In Figure 2 (right panel) we compare the total, aperture-corrected Ly α flux from the COS spectra, with the line intensity derived in ?. For the Ly α luminosity, we use the vignetting correction derived from the NUV images, as explained in Section 3. The comparison between the GALEX and COS measurements is informative, because the two instruments have different aperture size. The dashed lines in both panels indicates a factor of two difference in luminosity between the GALEX and COS measurements. It is interesting that for most of the galaxies the Ly α luminosity measured within the COS aperture is less than a factor of two fainter than the GALEX measurement, while the opposite is true for the UV luminosities. At face value, this result would indicate that the Ly α is more compact than the UV emission, in contrast with the strong evidence for more extended Ly α -emission in nearby and high- z galaxies presented by

???, e.g., . Given the uncertainty in the vignetting corrections we do not discuss this point any further.

4.2. Ly α profiles

In Figure 3 we show the profiles of the Ly α emission lines, centered on the galaxy systemic velocity derived using the H α emission line. The spectra are shown after 10 pixels (\sim XXXÅ) boxcar average. In two galaxies (GALEX1418+5259 and GALEX0959+0149) the Ly α line is very faint, and it is detected only after a rather heavy boxcar smoothing (\sim 0.7Å). The vertical dashed line in each panel shows the expected wavelength position of the Ly α based on optical-lines redshift measurements. In a clear majority of cases (\sim 20 of 25) the peak of the Ly α line is notably offset in wavelength to the red of the systemic velocity. In some cases multiple peaks are also visible, with a tendency (at least 10 cases) to show an additional peak on the blue side of the main peak, and also clearly bluewards of the systemic velocity. A handful of galaxies show additional red peaks that are clearly separated in three cases, and also extended bumps in the red wings of the primary line that could also be indicative of extended red features.

Using the measured wavelengths of the strongest Ly α emission peak, we compute the offsets relative to H α . These values are presented also in Table ?? and range generally between -50 and $+350$ km/s, with a mean velocity shift of 121 ± 18 km/s (standard error on the mean). We present this velocity distribution in the form of a histogram in Figure 4.

4.3. Continuum properties of the sample

The observations were designed to target the Ly α line, and consequently the continuum is not well exposed in individual galaxies. In Figure 5 we present the full COS spectra shifted into the rest-frame using the redshift measured from the H α emission line. The spectra are boxcar smoothed using a box of 1Å, and are shifted in the vertical direction for clarity. The horizontal dashed lines

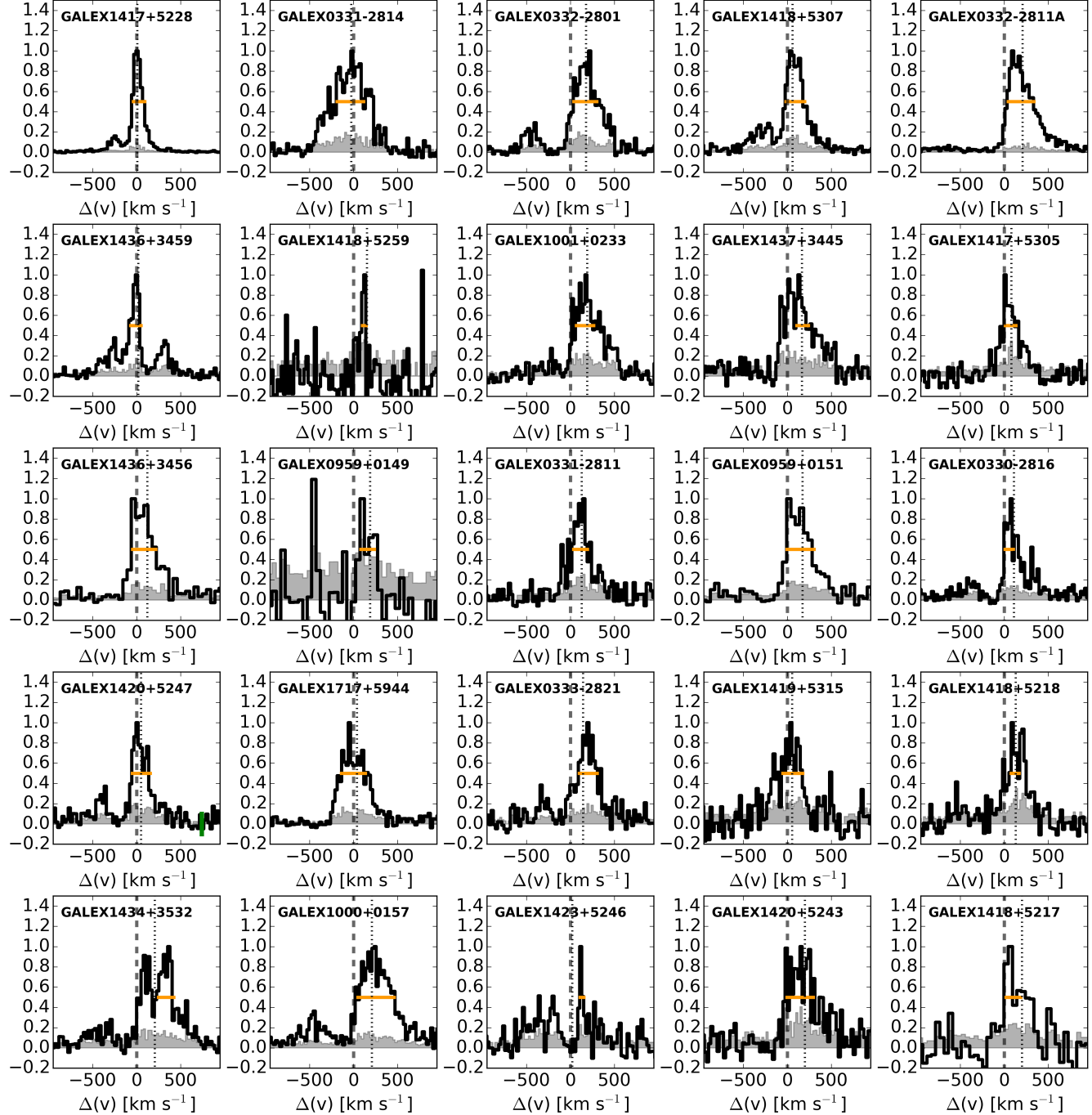


FIG. 3.— Rest-frame COS spectra of the 25 sample galaxies around the Ly α emission lines. The systemic velocity is determined from the nebular H α line. The spectra have been boxcar smoothed by 0.5Å.

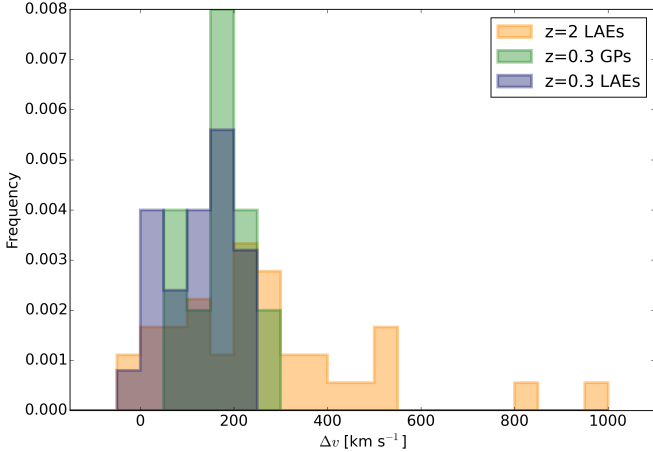


FIG. 4.— Histogram of the velocity difference between the Ly α and H α line. The black solid histogram shows the shifts for our GALEX LAEs at $z \approx 0.2$, while the blue histogram shows the offsets for $\langle z \rangle = 2.27$ LBGs from Steidel et al (2010). The arrow shows the shift of 104 km/s measured in the stacked spectrum shown in Figure ??.

show the zero flux level corresponding to each galaxy spectrum, while vertical lines mark the wavelength position of some prominent interstellar absorption features. Figure 5 shows that we are able to identify the strongest absorption feature only in a few individual sources, although the low S/N of the spectra prevent us from performing an accurate analysis.

Sample-averaged inferences can, however, be made through a stacking analysis. We blueshift the observed spectra into the rest-frame using the measured H α velocities. At every wavelength we compute a flux-weighted average and standard deviation. The mean stacked UV spectrum (shown after a box-car smoothing of 0.85Å) can be seen in Figure ??, where the shaded gray area corresponds to the weighted standard deviation, and the top panel shows the number of galaxies that entered the stack at each wavelength.

We are able to identify and clearly measure the features presented in Table 1 and marked in Figure ???. The list includes five lines that form in the ISM and one (CIII $\lambda 1175$) that is mainly photospheric. It is reassuring that the velocity shift of the CIII photospheric line is consistent with zero, as would be expected for young massive stars responsible of the ionization of the HII regions. The ISM lines, on the other hand, all show asymmetric absorption profiles, with the peak blueshifted outflow velocities in the range between 150–200 km s $^{-1}$.

5. DISCUSSION

5.1. Ly α output and UV surface density

Smaller galaxies tend to have larger Ly α EW (Figure 6), however, this does not seem to be a consequence of smaller galaxies having a higher UV surface density (Figure 7) surface density.

5.2. Lyman alpha scattering in galaxy outflows

It is frequently noted that Ly α , when found in emission, presents as a feature systematically redshifted from its systemic velocity (Kunth et al 1998, Shapley et al 2003, Tapken et al 2004, McLinden et al 2011). P Cygni-like Ly α profiles are thought to arise by scattering in

TABLE 1
ABSORPTION LINES MEASURED IN THE STACKED SPECTRUM.

Species	Formation	λ_{vac} Å	λ_{obs} Å	ΔV
H I Ly α	ISM	1215.67	1216.09	104.30
C III	Photo	1175.53	1175.37	-39 ± 41
Si II	ISM	1190.42	1189.83	-159.97
Si II	ISM	1193.29	1192.60	-173.39
Si III	ISM	1206.50	1205.87	-156.02
Si II	ISM	1260.42	1259.56	-205.19
Si II	ISM	1304.37	1259.56	-205.19
C II	ISM	1334.53	1333.81	-161.69

neutral gas that has been accelerated by mechanical energy returned from the star formation episode (Ahn & Lee XXX, Verhamme et al 2006). Our measured velocity shift for the interstellar absorption lines (150–200 km/s) places our stacked galaxy somewhere in the middle of the distribution for star-forming galaxies in the nearby universe selected for observation with HST (Leitherer et al 2011), suggesting they are not providing extreme feedback compared to their gas masses. Indeed the velocity shift of the LIS absorption lines compared with H α is also very similar to the sample average of 164 km/s measured in LBGs at $z \sim 2.7$ (Steidel et al 2010).

Regarding Ly α emission, radiative transport modeling has suggested that characteristic offsets to Ly α should exceed the blue-shifting of the neutral ISM offsets by factors of around two (Verhamme et al 2008). Measuring neutral ISM lines in faint Ly α -selected high- z galaxies is usually beyond the limits of the data in most LAE spectroscopic observations, but recently a number of Ly α velocity offsets have been measured with respect to H α and [OIII] lines: McLinden et al (2011) report offsets of 125 and 342 km/s for the two galaxies; Finkelstein et al (2011) report a 162 km/s offset in one galaxy and another that is consistent with zero; Hashimoto et al (2012) present four more galaxies with $\Delta v_{\text{Ly}\alpha}$ between 0 and 200 km/s; Guaita et al (submitted) present four more galaxies with offsets between 100 and 350 km/s. Our sample of 25 $\langle z \rangle = 0.2$ LAEs is twice the size of the combined samples at $z = 2 - 3$ and find a very similar distribution of Ly α velocity offsets, and suggests this offset to be somewhat characteristic of the Ly α -selected galaxy population, independent of redshift.

Similarly made measurements in continuum-selected galaxies at $z \sim 2.7$ find average absorption line offsets that match that measured in our stacked spectrum with surprising accuracy. It is of marked interest, therefore, that Ly α -H α offsets measured in the same sample of almost 100 LBGs (Steidel et al 2010, see also Kulas et al 2012) find a an average $\Delta v_{\text{Ly}\alpha}$ four times the value that we measure in the more nearby Universe. While the average offset of Ly α compared with the LIS lines for LBGs appears consistent with predictions from radiative transport models our average measurement of a Ly α offset significantly below the LIS offset is in stark contrast to predictions.

A plausible reconciliation of Ly α shifts below the outflow velocities of the oncoming gas may lie in exactly where in the HI medium Ly α obtains its redistribution in frequency. A measurement of the LIS lines will return

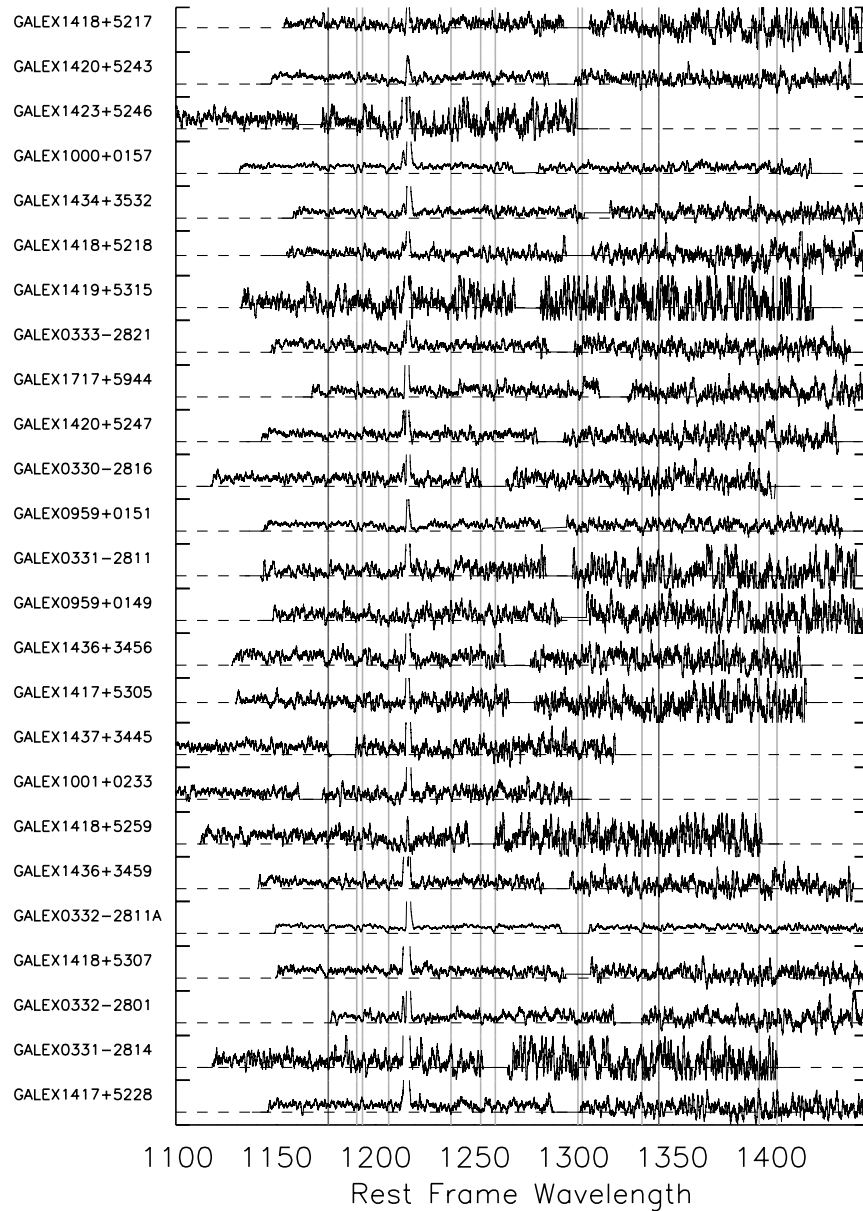


FIG. 5.— Rest-frame full NUV spectra of the 25 sample. The spectra are boxcar smoothed using a box of 1\AA , and are shifted in the vertical direction for clarity. The horizontal dashed lines show the zero flux level corresponding to each galaxy spectrum. Vertical lines mark the wavelength position of some prominent interstellar absorption features.

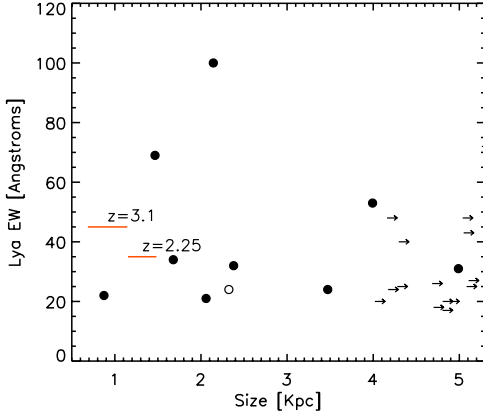


FIG. 6.— Ly α EW versus UV half light radius. Symbols as in previous figures. Horizontal red bars indicate the range of typical sizes of Ly α emitters at different redshift as indicated.

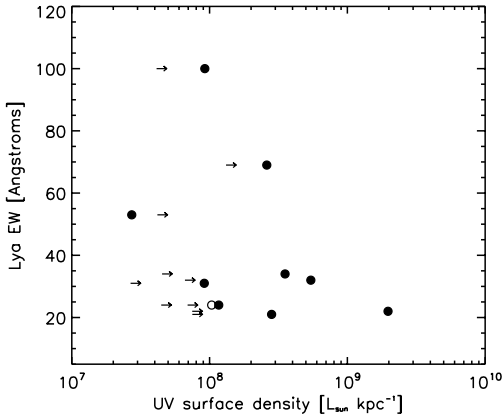


FIG. 7.— Ly α EW versus UV surface density. Symbols as in previous figures.

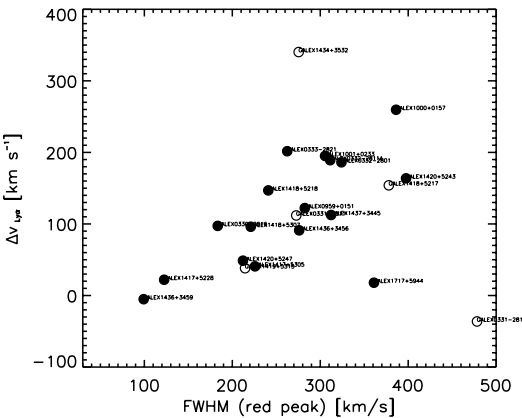


FIG. 8.— The Ly α -H α velocity shift compared with the line width of the red peak of the Ly α profile. Open circles indicates galaxies observed with MIRROR-B.

the velocity at which the column density of the absorbing species – and presumably also neutral hydrogen – is highest. For typical column densities in star-forming galaxies this may be on the order of 10^{20} cm^{-2} (Mas-Hesse et al 2003). In static gas, Ly α becomes optically

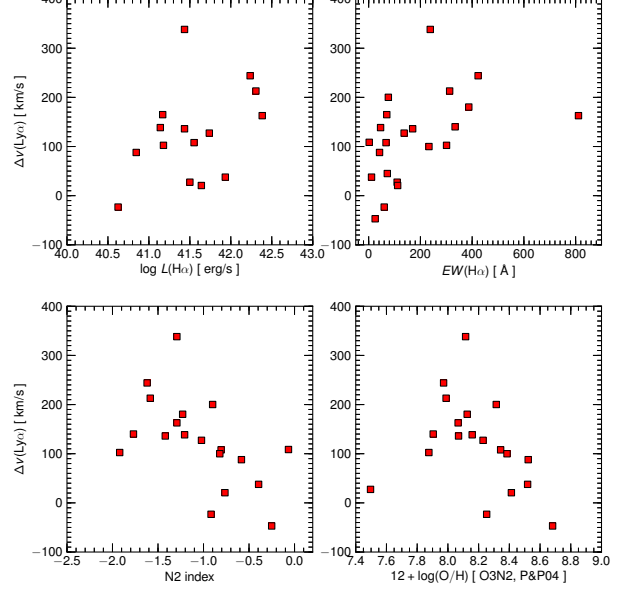


FIG. 9.— The Ly α -H α velocity shift compared with (a. *Upper left*) the H α luminosity; (b. *Upper right*) H α equivalent width; (c. *Lower left*) N2 index; (d. *Lower right*) gas phase metallicity

thick at column densities roughly 6 orders of magnitude below this value, which suggests that the gas responsible for the frequency distribution is both of lower column density and velocity than the bulk of the outflowing gas, and also resides closer to the recombination nebulae. Yet this scenario is not able to explain the marked difference seen between the Ly α and UV selected populations: why should the situation be different in the two populations? It is plausible also that we are observing the transition between Ly α photons that have been backscattered from receding shells (which must acquire around twice the velocity shift of the outflowing gas) and photons that are able to pass directly through the oncoming shell. The multiple peaking of many of the Ly α profiles is indeed also suggestive of this: indeed it appears that we are observing a large number of double-peaked profiles, in which the red peak is enhanced compared to the blue. From the available publications of transport modeling, this seems most resemblant of photon transfer and frequency redistribution in a single front-side medium.

5.3. What drives the velocity shift?

If the Ly α velocity shift is present, and the neutral gas observed to be accelerated, then one may expect the feedback to be coupled with other properties of the star-formation episode. Specifically, for example, outflows may be stronger in galaxies of higher SFR or specific SFR which in turn may manifest in larger velocity offsets. Adopting the H α luminosity as a proxy for SFR and its equivalent width as a rougher proxy for sSFR, we present the Ly α velocity shift compared with L(H α) and EW(H α) in the upper two panels of Figure 9.

The data present no such correlation of offset with SFR. Indeed while higher SFR must imply that more mechanical energy has been fed back to the ISM, it does not necessarily mean that the outflow would be faster. SFR and stellar mass are known to be strongly correlated in almost all galaxy samples, and should the neu-

tral gas mass also scale with stellar mass, proportionally more energy would be needed to drive a superwind of the same velocity. In this picture, a correlation with SFR would not be expected, but one would expect a stronger velocity offset when the SFR per unit mass, or sSFR, increases. Interestingly, then, the plot of $\Delta v(\text{Ly}\alpha)$ against $EW(\text{H}\alpha)$ shows a marked lower envelope consistent with this formulation. Galaxies with low equivalent widths ($\lesssim 100\text{\AA}$) can take the full range of outflow velocities (0 – 200 km/s), whereas galaxies with high sSFR ($EW(\text{H}\alpha) > 200 \text{\AA}$: eight of 22 measureable galaxies) present only with $\Delta v(\text{Ly}\alpha)$ above the sample average value of 100 km/s. It is plausible therefore, that since these galaxies have high SFR compared with their stellar mass, their SFRs may also be high compared with their neutral gas mass and are able to push the Ly α scattering medium to higher velocities.

From the optical spectra we also compute the N2 index [$\equiv \log_{10}([\text{[NII]}6584/\text{H}\alpha])$] and the gas-phase metallicity which we derive from the O3N2 index using the strong line calibration of calbiration of (Pettini & Pagel 2004). Here also there appears to be a rough anti-correlation between $\Delta v(\text{Ly}\alpha)$ and N2,O/H. However we note that the emission line measurements involve no quantitiy sensitive to the mass of the stellar population. Metallicity does, however, correlate strongly with stellar mass, implying that velocity shifts are somewhat higher in lower mass objects. This aligns well with the reasoning presented above, in explaining how a large range of offsets may be observed, despite showing no overall correlation with the total star formation rate.

5.4. How would a neutral Universe effect these observations?

In high-redshift studies, Ly α fluxes, number counts, luminosity functions, and asymmetries are all thought to be affected by the increasingly neutral fraction of hydrogen in the neutral IGM. However, disentangling possible IGM effects from those of the ISM has never been possible in these galaxy samples. In our $\langle z \rangle = 0.2$ observations we can perform a number of comparison studies on a set of observations for which we can be certain that the IGM has no influence on the Ly α line. We now proceed to examine how common assumptions about the IGM affect Ly α photometry and measurements of the profile asymmetry.

5.4.1. Photometry in an ionized and neutral universe

One of the primary use of the Ly α line in astrophysical cosmology is as a diagnostic of the reionization epoch, as an increasingly high fraction of intergalactic gas becomes neutral with increasing redshift (Miralda-Escude 1998; Haiman & Spaans 1999; Malhotra & Rhoads 2006; Kashikawa et al. 2006). Furthermore, should one want to derive the intrinsic Ly α output of a galaxy (before IGM attenuation) one needs to correct for the IGM. Indeed frequently, simple prescriptions (e.g. Madau 2005) for the IGM are applied directly to the Ly α line to make this correction (Cassata et al 2011; Blanc et al 2011), which accounts for almost 50% of the Ly α flux at $z = 6$. This is the entire premise for the recent claim of an extremely high EW Ly α emitter at $z = 6.5$ (Kashikawa et al 2012). These corrections include two major unknown

questions: by how much is the Ly α line offset redward of its systemic velocity? and how close do the Ly α forest clouds really come to the Ly α line? With these data we have already answered the former question, and we will now proceed with a simple assessment of how common assumptions of the latter may affect conclusions.

Using the systemic redshift for our sample as measured by H α and the canonical prescription for intergalactic Lyman series line blanketing of Madua (1995), we simulate or Ly α spectra in the common redshift windows of $z = 5.7$ and 6.5 . We simply blueshift the galaxies to $z = 0$ and redshift them to the high-z windows, apply the IGM, and re-compute the luminosities using the same method as in Table ???. We present the luminosities, both unattenuated and suppressed by the $z = 5.7$ and 6.5 IGM, in Table 3, and make a graphical comparison in Figure 10.

Immediately it can be seen that the simulated high-z luminosities lie very close to the total measured fluxes. Only in a handful of cases – obviously the few galaxies with symmetric Ly α lines centred around the systemic velocity – is there a significant suppression of the Ly α line by the IGM. Indeed the majority of Ly α profiles shown in Figure 5 are noteably redshifted, with only a small component to the total flux provided by the blue peak. The effect of the IGM is essentially to completely remove the blue peak but leave the redshifted, dominant peak almost completely unaffected. We compute the average values of $L(\text{Ly}\alpha, \text{IGM}) / L(\text{Ly}\alpha, \text{noIGM})$, which evaluates to 0.81 ± 0.17 (standard error on the mean) at both tested redshifts. It is possible that additional flux could be suppressed by the red damping wing of a neutral IGM that has not been accounted for by these models. This would further suppress our Ly α luminosities in the simulated spectra, but it should be noted that this is not usually accounted for either by high-z observational studies. The damping wing would have equal additional effect on high-z data and these simulations. With so many galaxies lying close to the 1:1 line, we find no argument for doubling observed $z \gtrsim 6$ fluxes, especially in individual cases. This conclusion is also supported by the fact that asymmetries do not differ at high- and low-z, as we will discuss in the next section.

5.4.2. Ly α asymmetry in an ionized universe

As well as applying a redward velocity offset to the transferred Ly α line, scattering in netural gas is also well-known to introduce asymmetries to the profile itself. In the spectra of high-z galaxies, when spectral resolution permits, Ly α almost ubiquitously presents asymmetrically (Shapley et al 2003; Kurk et al. 2004; Shimasaku et al 2006) and, at the highest redshifts, is expected to be enhanced by neutral gas in the IGM. Indeed, quantitative measurements of the profile asymmetry have also been invoked to discriminate between Ly α emitting galaxies and foreground interlopers (e.g. [OII] emitters where the line is not subject to radiative transport effects; Kashikawa et al 2006). As with the transmitted line flux, however, the effect that the IGM has on the transmitted line is strongly dependent upon how close the IGM comes to the Ly α line that is transported through the ISM.

Our well resolved and high S/N COS observations give us the possibility to compute quantitative asymmetries for a sample of Ly α selected galaxies in which we can

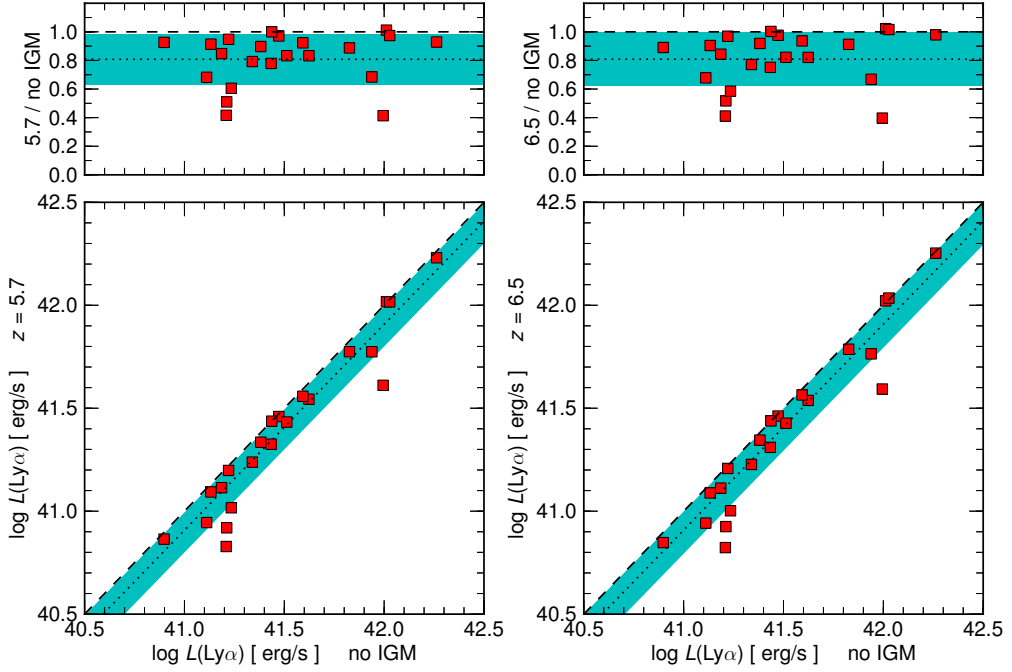


FIG. 10.— Comparison of the measured luminosity of Ly α , with the same measurements when the spectra have been ‘absorbed’ by the standard Madau (1995) IGM prescription assuming redshift $z = 5.7$ (left) and $z = 6.5$ (right). The lower panels show a direct comparison of the luminosities, while the upper panels show the fractional luminosity that is transmitted through the IGM. By eye the left and right plots are indistinguishable. The dotted lines show the average ratios of $L\{5.7, 6.5\} = 0.81L(z = 0)$, which differ only at the fourth significant digit. Shaded regions show the standard error on the mean, which is almost consistent with the 1:1 line.

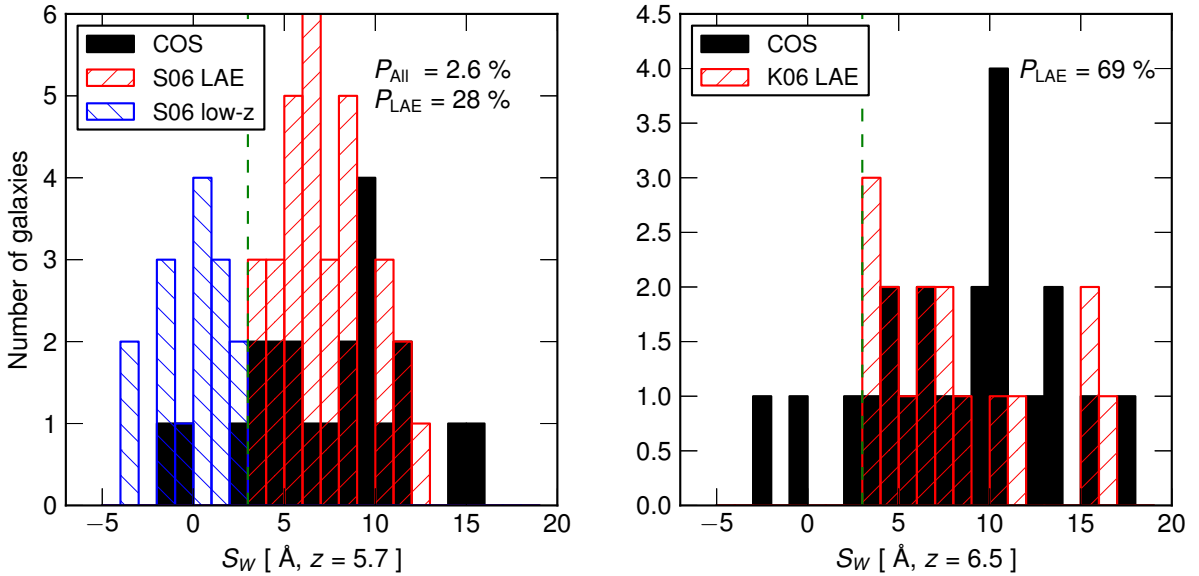


FIG. 11.— Distribution of the weighted skewness S_W of our COS Ly α profiles. Histograms of our own sample are presented in black, scaled in redshift to $z = 5.7$ (left) and $z = 6.5$ (right). Overplotted in the left panel are the LAEs from Shimasaku et al (2006) in red, and the emission line objects determined to be lower redshift interlopers in blue. In the right panel the red histogram shows the LAEs of Kashikawa et al (2006). Labeled in the figures are the probabilities that the high- z samples ($z = 5.7$ LAEs, LAEs+interlopers, and $z = 6.5$ LAEs) are drawn from the same parent population using the K -sample Anderson-Darling rank sum comparison. It shows the LAEs populations to be indistinguishable but LAE+interlopers are clearly unlikely to share an underlying distribution.

say with certainty that the frequency redistribution occurs inside the ISM. We opt to measure profile skewness (Kurk et al 2004), ‘weighted skewness’ (Shimasaku et al 2006) and red/blue ratios of the peak-to-10% wavelength and flux (Rhoads et al 2003). We are able to perform these

measurements in 22 of our 25 objects, and present the results in Table 3.

Firstly regarding weighted skewness, the index has been used by Shimasaku et al (2006) at $z = 5.7$ and Kashikawa et al (2006) at $z = 6.5$ to cull interloping

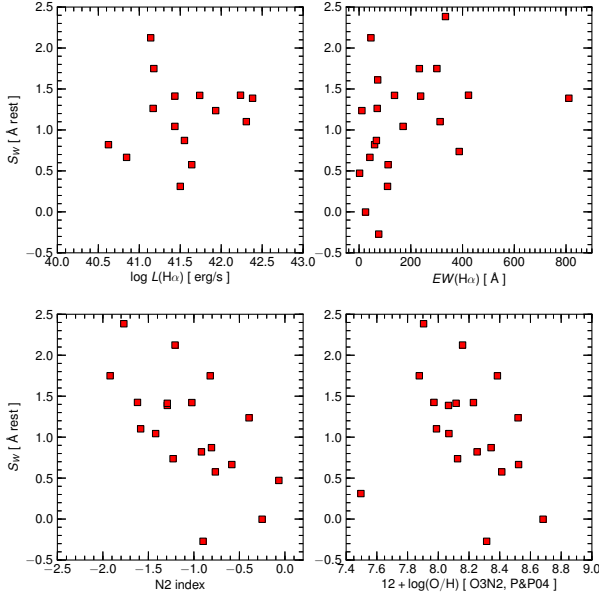


FIG. 12.— Same as Figure 9 but with weighted skewness, S_W . galaxies from their sample, by invoking a threshold S_W of > 3 to select LAEs. Scaling our measurements of S_W into the observer frame at these redshifts we present histograms of the S_W for the COS sample in Figure 11. Overplotted are the LAE and low- z samples of Shimasaku, and LAEs measured and compiled in Kashikawa et al. It is immediately clear from these histograms that our GALEX-selected LAEs exhibit a very similar range of S_W to both high- z LAEs samples, whereas the interloping sample of Shimasaku et al (2006) shows very little clear overlap. In order to assess this similarity quantitatively, we employ a K -sample Anderson–Darling (1952) rank sum comparison⁹. Indeed for the two LAE samples, data are consistent with the null hypothesis (that the two samples are drawn from the same parent distribution) at only the 28% level ($z = 5.7$) and 69% ($z = 6.5$) level. However the same test performed on the concatenated LAE+interloper sample at $z = 5.7$ suggests there is a $< 3\%$ chance the two samples share the same parent distribution, and the selection of $S_W > 3$ as invoked in those studies seems appropriate. It seems likely, however, that the asymmetry is introduced by the scattering of Ly α photons within the ISM of these galaxies and not by an encroaching neutral IGM. If the IGM does not have an appreciable effect on the asymmetry of the Ly α line at high- z it must reflect the fact that the Ly α forest does not come close enough to Ly α to sufficiently affect the blue wing, possibly because of redshifting within the ISM, which is certainly very consistent with a reduction in flux of only $\sim 20\%$ as shown in the previous Section. If it has an effect at all, it must be very grey, and likely be caused only by the damping wing.

6. SIMPLE MODEL FOR THE NEUTRAL GAS KINEMATICS

==; outflows a grandi distanze? ==; prochaska non trova il transverse proximity effect. ==; Ly α nebulae su

⁹ The A–D test is similar to the frequently adopted KolmogorovSmirnov (K–S) test but considers the full range of data values as opposed to the largest single deviation, and is therefore more robust against strong biases from outlying points.

scale

6.1. Mass outflow rate

We can use the best-fit parameters for the asymmetric outflow model to estimate the average mass outflow rate (\dot{M}) in Ly α emitters. For a mass flux, and assuming that the absorbing material has a covering fraction of one, the mass density at r can be written as a function of the gas velocity and mass loss rate (\dot{M}) through the solid angle Ω (e.g., ?):

$$\rho(v) = \frac{\dot{M}}{\Omega v r^2}. \quad (2)$$

At $r = R_{SF}$ we have $\dot{M} = \rho_{R_{SF}} \Omega v_0 R_{SF}^2$. The density in the above Equation is the total gas density ($\rho = n_H m_H (1 + 4Y_{He})$, where m_H is the mass of the hydrogen atom, and Y_{He} is the relative abundance by number of He with respect to hydrogen).

The hydrogen number density (n_H) can be derived from the number density of Si $^{+}$ if the Si $^{+}$ ionization fraction ($\chi(r)$), relative abundance with respect to hydrogen ($A(r)$), and finally its depletion fraction on dust grains (D) are known. We can write:

$$n_{0,H} = \frac{n_{0,\text{Si}^{+}}}{\chi A D}, \quad (3)$$

where the subscript 0 indicates that the quantities are computed at R_{SF} . We proceed to compute $n_{0,\text{Si}^{+}}$ from the best-fit value of τ_0 (see Eqn ??). The UV sizes were computed using the COS NUV acquisition images, and range between 0.5 and 4.6 kpc, with an average value of $R_{SF} = 2.1$ kpc. Assuming the average value for R_{SF} , we find $n_{\text{Si}^{+}} \approx 4.4 \times 10^{-7} \text{ cm}^{-3}$.

The depletion of Si on dust grain is uncertain. However, it is probably low in the high velocity gas probed by our study (see ?, for depletion values in high velocity clouds in the Milky Way). We set $D = 1$ in our calculations.

For the Ly α emitting galaxies included in the stacked spectrum optical spectroscopy was obtained to constrain the metal content in the ionized-gas. Following (?), we used the $N2$ parameter ($N2 = \log(f(\text{[NII]}\lambda6584)/f(\text{H}\alpha))$), together with the ? calibration derived from local galaxies. The average $N2$ in the sample galaxies is -1.1 ± 0.6 , corresponding to an oxygen abundance of $12 + \log(O/H) = 8.26 \pm 0.34$ (i.e, approximately one third solar, ?). We assume that the metallicity of the outflowing material probed by the [Si II] absorption is the same of the ionized gas probed by the H α emission. There is, however, the possibility that the current star formation episode is fueled by low metallicity gas accreted from the IGM. In this case, the outflow could potentially have a larger metallicity and 1/3 solar can be interpreted as a lower limit. From the solar photospheric abundance of Si relative to H given in ?, $n_{\text{Si}}/n_H = 3.2 \times 10^{-5}$, we adopt $A = 1.1 \times 10^{-5}$.

We can constrain the ionization state of Si (χ) from the numerical density of Si $^{++}$. The latter can be estimated from the observed [Si III] resonant transition at 1206Å. As shown in Figure ?? the profile around 1206Å is of pure absorption, blueshifted with respect to systemic velocity by $188 \pm 20 \text{ km s}^{-1}$. We can reproduce this absorption

TABLE 2
LY α PROPERTIES

Galaxy	Ly α luminosity	λ_B	λ_R	Morphology	Notes
	10^{42} erg s $^{-1}$	Å			
GALEX1417+5228	1.38 ± 0.03	1467.93 ± 0.01	1469.15 ± 0.01	0	
GALEX0331-2814 ^a	1.30 ± 0.05	...	1556.30 ± 0.10	2	
GALEX0332-2801	0.39 ± 0.02	1475.82 ± 0.01	1478.90 ± 0.01	0	
GALEX1418+5307	0.53 ± 0.02	1462.12 ± 0.01	1463.68 ± 0.03	0	
GALEX0332-2811A	1.06 ± 0.02	...	1465.08 ± 0.01	2	
GALEX1436+3459	0.38 ± 0.02	1473.83 ± 0.01	1474.98 ± 0.01	0	
GALEX1418+5259	0.04 ± 0.02	0	
GALEX1001+0233	1.83 ± 0.14	...	1682.10 ± 0.01	1	
GALEX1437+3445	0.83 ± 0.07	...	1610.23 ± 0.01	1	
GALEX1417+5305	0.31 ± 0.03	...	1541.07 ± 0.01	1	
GALEX1436+3456	0.59 ± 0.04	...	1543.24 ± 0.01	1	
GALEX0959+0149	0.02 ± 0.00	1	
GALEX0331-2811 ^a	0.17 ± 0.01	...	1474.29 ± 0.10	1	
GALEX0959+0151	0.29 ± 0.02	...	1521.75 ± 0.01	2	
GALEX0330-2816	0.52 ± 0.04	1555.92 ± 0.01	1558.40 ± 0.01	2	
GALEX1420+5247	0.40 ± 0.03	1520.95 ± 0.01	1523.22 ± 0.01	0	
GALEX1717+5944	0.24 ± 0.01	...	1453.92 ± 0.01	1	
GALEX0333-2821	0.37 ± 0.03	1515.08 ± 0.01	1517.56 ± 0.01	2	
GALEX1419+5315 ^a	0.25 ± 0.02	1535.93 ± 0.10	1536.80 ± 0.10	1	
GALEX1418+5218	0.22 ± 0.02	...	1507.02 ± 0.01	1	
GALEX1434+3532 ^a	0.16 ± 0.01	1453.15 ± 0.10	1454.12 ± 0.10	2	
GALEX1000+0157	1.23 ± 0.05	1535.20 ± 0.01	1538.83 ± 0.03	2	
GALEX1423+5246	0.36 ± 0.05	1632.31 ± 0.01	1634.03 ± 0.01	0	
GALEX1420+5243	0.11 ± 0.01	...	1517.26 ± 0.01	1	
GALEX1418+5217	0.07 ± 0.01	...	1508.37 ± 0.01	1	

^a Galaxy observed with MIRRORB

profile with the same best-fit gas geometry, density and velocity fields derived from the [Si II] doublet, only if we do not include the scattered blue emission (the dotted line in Figure ?? shows the model including the blue scattered re-emission). This possibly indicates that the ratio Si⁺⁺/Si⁺ is not constant in the envelope, and thus Si⁺ and Si⁺⁺ may have different radial density profiles. Neglecting the blueshifted re-emission results in an underestimate of the Si⁺⁺ density, by a factor of a few. The best-fit absorption profile is shown in Figure ?? (blue line). With the same $R_{SF} = 2$ kpc assumption, we find $n_{\text{Si}^{++}} \approx 1.8 \times 10 \times 10^{-7} \text{ cm}^{-3}$, so that $n_{\text{Si}^+} \approx 3 \times n_{\text{Si}^{++}}$. Thus, we take $\chi = XXX$ in the calculation of the total gas density. We also note that, given the relative ionization potentials of Si (8.16 eV) and Si⁺ (16.3 eV) compared to H, the measured $n_{\text{Si}^+}/n_{\text{Si}^{++}}$ ratio also implies that the observed absorption is associated with hydrogen in neutral form, and thus the Si⁺ ions trace the neutral phase of the wind around the star-forming regions.

Following the above discussion, we obtain a neutral hydrogen number density at R_{SF} of 0.12 cm^{-3} , and a corresponding mass outflow rate from Eqn 2 $\dot{M} \approx 6M_{\odot} \text{ yr}^{-1}$.

From the mass outflow rate computed above and the

galaxies' average star-formation rate (SFR), we can constrain the outflow mass loading factor ($\eta = \frac{\dot{M}}{SFR}$?). In galaxy formation models, this parameter is used to quantify the strength of ejective feedback, which regulates both the shape of the mass-metallicity relation, as well as the stellar mass growth rate of low mass haloes (??). Theoretical analysis reproducing the $Z - M$ scaling currently favor $\eta \propto M_*^{-1/3}$, as expected from momentum-driven winds. However, the value of η and its dependence on redshift and galaxy halo mass are still poorly constrained observationally (e.g. ?).

All galaxies in the sample have measured H α and H β luminosities from ???. We corrected the observed H α luminosities for the dust extinction derived from the Balmer ratio, following ?. The average extinction corrected H α luminosity for the sample galaxies is $L_{H\alpha, \text{intr}} = 2 \times 10^{42} \text{ ergs s}^{-1}$, corresponding to a star formation rate (SFR) of $5.3 M_{\odot} \text{ yr}^{-1}$ (?). Consequently, the average mass outflow rate is comparable to the average SFR of the galaxies, implying a mass loading factor $\eta \approx 1$.

7. CONCLUSIONS

APPENDIX

TABLE 3
LY α PROPERTIES

Galaxy	$L(\text{Ly}\alpha)$ $z \approx 0.2$	$L(\text{Ly}\alpha)$ $z = 5.7$	$L(\text{Ly}\alpha)$ $z = 6.5$	S	S_W restframe	a_λ	a_f
			$10^{42} \text{ erg s}^{-1}$		Å		
GALEX1417+5228	0.8683452	0.59431674	0.58045145	0.3257	0.3111	1.3911	1.1336
GALEX0331-2814	0.9879125	0.40850181	0.39195428	-0.0005	-0.0019	1.1200	1.1664
GALEX0332-2801	0.2968061	0.28822474	0.28972307	0.3302	0.7366	1.4548	1.1182
GALEX1418+5307	0.3253785	0.27104907	0.26745902	0.7069	1.7490	1.9388	1.2733
GALEX0332-2811A	1.0268168	1.03903657	1.04980441	0.7829	2.3841	3.2959	2.5272
GALEX1436+3459	0.1617906	0.06735962	0.06653605	0.2157	0.8201	1.1572	1.0255
GALEX1418+5259
GALEX1001+0233	1.8302378	1.70001528	1.79157804	0.4425	1.1013	1.4782	0.9778
GALEX1437+3445	0.6702077	0.59474476	0.61162917	0.5168	1.4220	1.6727	1.0336
GALEX1417+5305	0.2185427	0.17312553	0.16863250	0.2683	0.6653	1.1339	0.9910
GALEX1436+3456	0.4200032	0.34970323	0.34498662	0.4187	0.8716	1.3015	1.0307
GALEX0959+0149
GALEX0331-2811	0.1290824	0.08804660	0.08752134	0.2148	0.4716	1.2907	1.1101
GALEX0959+0151	0.2410013	0.21624882	0.22142958	0.5152	1.3871	1.5846	0.9668
GALEX0330-2816	0.3915936	0.36145186	0.36668307	0.7417	1.7484	2.3003	1.2957
GALEX1420+5247	0.2715689	0.21156661	0.20416373	0.7195	1.6103	1.7882	1.0904
GALEX1717+5944	0.1627919	0.08300855	0.08414941	0.2319	0.5756	1.2347	0.8833
GALEX0333-2821	0.2735889	0.27358894	0.27433189	-0.1404	-0.2713	0.8893	0.9822
GALEX1419+5315	0.1716515	0.10385135	0.10045273	0.3076	1.2359	1.0930	1.0538
GALEX1418+5218	0.1356059	0.12393059	0.12262569	0.3782	1.0433	1.3154	1.0743
GALEX1434+3532	0.1663425	0.15767323	0.16124933	0.3799	1.4133	1.1025	0.6788
GALEX1000+0157	1.0665986	1.03887225	1.08392759	0.4636	1.4241	1.8650	1.2989
GALEX1423+5246
GALEX1420+5243	0.1534203	0.13006413	0.12941483	0.4176	1.2627	1.6465	1.2509
GALEX1418+5217	0.0789956	0.07316467	0.07035331	0.6654	2.1243	1.6930	1.0659

TABLE 4
ATOMIC DATA FOR Si II ION.

Vac. Wavelength Å	A_{ul} s^{-1}	f_{lu}	$E_l - E_u$ eV	$g_l - g_u$	Lower level Conf., Term, J	Upper level Conf., Term, J
1190.42	6.53×10^8	2.77×10^{-1}	0.0 – 10.41520	2 – 4	$3s^2 3p\ 2P^0\ 1/2$	$3s 3p^2\ 2P\ 3/2$
1193.28	2.69×10^9	5.75×10^{-1}	0.0 – 10.39012	2 – 2	$3s^2 3p\ 2P^0\ 1/2$	$3s 3p^2\ 2P\ 1/2$
1194.50	3.45×10^9	7.37×10^{-1}	0.035613 – 10.41520	4 – 4	$3s^2 3p\ 2P^0\ 3/2$	$3s 3p^2\ 2P\ 3/2$
1197.39	1.40×10^9	1.50×10^{-1}	0.035613 – 10.39012	4 – 2	$3s^2 3p\ 2P^0\ 3/2$	$3s 3p^2\ 2P\ 1/2$